Paper II

Spatiotemporal Long-Range Persistence in Earth's Temperature Field: Analysis of Stochastic-Diffusive Energy Balance Models

Spatiotemporal Long-Range Persistence in Earth's Temperature Field: Analysis of Stochastic–Diffusive Energy Balance Models

Kristoffer Rypdal, Martin Rypdal, and Hege-Beate Fredriksen

Department of Mathematics and Statistics, UiT The Arctic University of Norway, Tromsø, Norway

ABSTRACT

A two-dimensional stochastic–diffusive energy balance model (EBM) formulated on a sphere by G. R. North et al. is explored and generalized. Instantaneous and frequency-dependent spatial autocorrelation functions and local temporal power spectral densities are computed for local sites and for spatially averaged surface temperature signals up to the global scale. On time scales up to the relaxation time scale given by the effective heat capacities of the ocean mixed layer and land surface, respectively, scaling features are obtained that are reminiscent of what can be derived from the observed temperature field. On longer time scales, however, the EBM predicts a transition to a white-noise scaling, which is not reflected in the observed records. A fractional generalization, which can be considered as a spatial generalization of the zero-dimensional, long-memory EBM of M. Rypdal and K. Rypdal, is proposed and explored. It is demonstrated that this generalized model describes qualitatively the main correlation characteristics of the temperature field reported in the literature and those derived herein from 500-yr-long control simulations of the NorESM Earth system model. A further generalization of the model, to include long-term persistence in the stochastic forcing, is also discussed.

1. Introduction

The enormous complexity of present-day general circulation climate models implies that model data can only be interpreted through advanced data analysis. Implicit in such data analysis is always the application of concepts based on simpler dynamic, stochastic–dynamic, or statistical model frameworks. Such models will in some form describe the correlation structure of Earth's climatic fields. Zero-dimensional energy balance models (EBMs) only describe correlation structure in time—in simplest form, as an exponential relaxation time with a time constant of a few years determined by the heat capacity of the ocean mixed layer. Zero-dimensional two-layer models include the energy exchange between the mixed layer and the deep ocean, which introduces another and larger time constant of the order of a century (Held et al. 2010; Geoffroy et al. 2013). An alternative generalization of

the one-layer model, which yields a power-law impulse response, was introduced by Rypdal (2012) and, by further introducing stochastic forcing, in Rypdal and Rypdal (2014). These generalizations thus provide a phenomenological stochastic–dynamical model describing the long-range temporal correlation structure on time scales from years to centuries observed in global temperature data as well as in millennium-long climate model simulations (Østvand et al. 2014).

One-dimensional EBMs describe meridional energy transport in addition to the vertical radiation balance (Budyko 1969; Sellers 1969), and two-dimensional models include also zonal transport. There is a plethora of papers on such models, many of which include a stochastic forcing. One of the earlier studies of such stochastic-diffusive EBMs was made by North and Cahalan (1981). This model was expanded to include a simple model for ocean diffusion and upwelling by Kim and North (1992), and was compared to early versions of atmospheric–ocean general circulation models (AOGCMs) by Kim et al. (1996). The latter study revealed power-law temporal spectra corresponding to strong long-range temporal correlation structure in global temperature on time scales up to a decade in the AOGCMs, but a loss of correlations on longer time scales. The stochastic–diffusive EBM showed a more gradual transition toward uncorrelated noise on longer time

---

scales. Their spectra of instrumental global temperature also shows the transition to uncorrelated noise on time scales longer than a decade, which is now known not to reflect the true correlation structure on time scales from decades to centuries revealed in millennium-long temperature reconstructions (Rypdal et al. 2013) and AOGCM simulations (Østvand et al. 2014). The explanation of the observed flattening of the spectra on long time scales may be the particular spectral analysis method used in Kim et al. (1996), which is based on fitting a high-order autoregressive (AR) process to the data. AR processes cannot model long-range dependence in data (Beran 1994).

The work presented in the present paper focuses on the more fundamental mechanisms by which spatiotemporal long-range persistence may arise in Earth's temperature field. Hence the goal is not to construct a model that reflects the details in land–ocean topography, and parameters in the model are estimated from data, not derived from modeling the actual physics. It is inspired by, and a generalization of, the recent work by North et al. (2011). In that paper the stochastic–diffusive EBM is first formulated on a plane disk, where it takes the form

$$\tau_r \frac{\partial T}{\partial t} + T - \lambda^2 \left(\frac{\partial^2 T}{\partial x^2} + \frac{\partial^2 T}{\partial y^2} \right) = F(t, x, y). \qquad (1)$$

Here t is time, x, y are the two spatial coordinates, $T(t, x, y)$ is the surface temperature field, and τ_r is a relaxation time constant that is proportional to the effective heat capacity per unit area of the surface and inversely proportional to the effective emissivity of outgoing longwave radiation. Also, $F(t, x, y)$ represents the horizontal turbulent energy flux into a vertical column of unit area due to atmospheric weather systems, and the standard choice is to model it as a white-noise source field in space and time. The generalization of this equation to the surface of a sphere is straightforward, and is done in North et al. (2011). The assumptions of isotropy and the uniformity of the diffusion tensor are obviously unrealistic, since it ignores the meridional dependence of the insolation and the uneven distribution of landmasses. This distribution also affects the time constant τ_r since the heat capacity of the ocean mixed layer is much larger than that of the land surface.

It is shown in North et al. (2011) that the stationary random field resulting from Eq. (1) exhibits an exponentially decaying, frequency-dependent, spatial autocorrelation function (ACF). They express this as a frequency-dependent spatial autocovariance $C_\omega(r)$ defined as the inverse spatial Fourier transform (FT) of the space–time spectral density $S_{\omega, \mathbf{k}} = E[|T_{\omega, \mathbf{k}}|^2]$. Here $T_{\omega, \mathbf{k}}$ is the space–time FT of the temperature field and $E[\cdot]$ denotes the expectation value. They give an analytic expression for $C_\omega(r)$ on the flat disk, which in the limit $r/\lambda \to \infty$ decays

exponentially in space with a correlation length λ_ω that decreases with increasing ω. In the limit $\omega \to 0$ the correlation length is $\lambda_0 = \lambda$. This means that the spatial ACFs are short-range (exponential rather than power law), and that this model cannot describe long-range spatial correlations.

North et al. (2011) do not compute explicit instantaneous spatial ACFs or temporal power spectral densities (PSDs). From a data-analysis viewpoint temporal spectra are of great interest because of the published evidence that such spectra exhibit power-law scaling of the form $S(\omega) \sim \omega^{-\beta}$ with $\beta \in (0, 1)$ both for local and globally averaged temperature records (Rypdal et al. 2013; Rypdal and Rypdal 2014; Østvand et al. 2014). The spectral index β measures the degree of persistence in the record, and in local records it is close to unity over oceans, and close to zero over land (Fraedrich and Blender 2003). It also appears that β is larger in records averaged over large areas, like global and hemispheric averages, than in local time series. As we will demonstrate in section 2, many of these features are described by the stochastic-diffusive EBM of North et al. (2011) (in the following called the North EBM) for time scales up to the relaxation time τ_r. However, we also show that persistent long-range correlations beyond this time scale cannot be described by this model. In section 3 we generalize this model to include long-memory delays in the surface temperature response due to energy exchange between the ocean mixed layer and the deep ocean. Mathematically this is done by replacing the exponential temporal relaxation due to vertical radiative energy balance with a power-law relaxation (Rypdal and Rypdal 2014), and corresponds to introduction of a fractional time derivative in the North EBM (Rypdal 2012). We demonstrate the power-law nature of spatiotemporal correlations in this model and its consistency with an observed reconstructed temperature time series. In section 4 we compare these results with multicentury long control simulations of the NorESM Earth system model and find that the fractional EBM provides a better description of the correlation structure observed in these simulations than the North EBM. Transient relaxation after a sudden increase in forcing in the NorESM shows a long-range persistent response, but with a lower β than observed in the control simulations. This motivates a generalization of the fractional EBM to include persistent, stochastic forcing in section 5. In section 6 we summarize and conclude, and in the appendixes we elaborate on some mathematical technicalities.

2. The North EBM on a sphere

a. Spatial ACFs and temporal PSDs of the North EBM

In this section we shall outline the derivation of the frequency-dependent spatial ACF given by North et al.

(2011) and then derive the corresponding temporal PSD for a time series measured in a given location on the sphere. On the unit sphere Eq. (1) for the temperature field $T(t, \mu, \phi)$ takes the form

$$\tau_r \frac{\partial T}{\partial t} + T - \lambda^2 \frac{\partial}{\partial \mu}\left[(1 - \mu^2)\frac{\partial T}{\partial \mu}\right] - \frac{\lambda^2}{1 - \mu^2}\frac{\partial^2 T}{\partial \phi^2} = F(t, \mu, \phi),$$ (2)

where $\mu = \cos\theta$, where θ is the polar angle, and ϕ is the azimuthal angle (longitude). This equation is now formulated on the rectangle $\mu \in [-1, 1]$, $\phi \in [0, 2\pi)$. To avoid all the subtleties of stochastic integrals we shall start by representing the random forcing field $F(t, \mu, \phi,)$ by a finite series $F_{K,N}(t, \mu, \phi)$ of spherical harmonics $Y_{n,m}(\mu, \phi)$ in space and harmonic functions $\exp(i\omega_j t)$ in time:

$$F_{K,N}(t, \mu, \phi) = \sum_{j=-K/2}^{K/2} \sum_{n=0}^{N} \sum_{m=-n}^{n} F(\omega_j, n, m)e^{i\omega_j t} Y_{n,m}(\mu, \phi).$$ (3)

Here $\omega_j = 2\pi j$, $j = -K/2, \ldots, K/2$, are the frequencies of the discrete Fourier expansion of a time series with $K + 1$ elements sampled at intervals $\Delta t = 1/K$ (the time record is supposed to have duration $K\Delta t = 1$). We shall let the integers $K, N \rightarrow \infty$ at the end, which corresponds to the continuum limit $\Delta t \rightarrow 0$ in time and also infinite spatial resolution on the sphere. In appendix A it will be shown that if $F(t, \mu, \phi)$ is a random field (a white-noise process in space and time) the variance of the expansion coefficients will be the same for all terms in the sum, that is,

$$E[|F(\omega_j, n, m)|^2] = \sigma^2,$$ (4)

for all $-K/2 \leq j \leq K/2$ and $0 \leq n \leq N$. Higher spatiotemporal resolution is obtained by increasing K and N, and since all spatiotemporal scales are represented by equal power in the random field the total power diverges as $K, N \rightarrow \infty$. This power now takes the form

$$\mathcal{P}_{K,N} = \int_0^1 dt \int_{4\pi} d\Omega\, E[|F_{K,N}(\mu, \phi, t)|^2],$$

where $d\Omega = \sin\theta\, d\theta\, d\phi = -d\mu\, d\phi$ is the solid angle differential. Inserting Eq. (3) into this integral, using the orthonormality of the basis functions $Y_{n,m}(\mu, \phi)$ and $\exp(i\omega_j t)$, and the random-field assumption Eq. (4), we find after some straightforward algebra

$$\mathcal{P}_{K,N} = (K + 1)(N + 1)^2 \sigma^2.$$ (5)

By expanding the temperature field in the same way as the forcing field in Eq. (3), and substituting these expansions into Eq. (2), we find

$$T(\omega, n, m) = \frac{F(\omega, n, m)}{-i\omega\tau_r + \lambda^2 n(n + 1) + 1},$$ (6)

and hence

$$T(\omega, \mu, \phi) = \sum_{n=0}^{\infty} \sum_{m=-n}^{n} \frac{F(\omega, n, m)Y_{n,m}(\mu, \phi)}{-i\omega\tau_r + \lambda^2 n(n + 1) + 1}.$$ (7)

This formula can be used for computing the frequency-dependent spatial ACF as well as the temporal PSD. The frequency-dependent covariance between the "North pole" given by the unit vector $\hat{\mathbf{z}}$ (given by $\mu = 1$) and the point $\hat{\mathbf{r}}$ (given by μ, ϕ) is defined by

$$C_\omega(\hat{\mathbf{r}}, \hat{\mathbf{z}}) = C_\omega(\mu) = E[T(\omega, \mu, \phi)T^*(\omega, 1, 0)].$$ (8)

Because of the statistical uniformity of the fields on the sphere this is the covariance between any two points $\hat{\mathbf{r}}$ and $\hat{\mathbf{r}}'$ separated by an angle α such that $\mu = \cos\alpha = \hat{\mathbf{r}} \cdot \hat{\mathbf{r}}'$. By inserting Eq. (7) into Eq. (8), using the white-noise relation

$$E[F(\omega, m, n)F^*(\omega, m', n')] = \sigma^2 \delta_{m,m'}\delta_{n,n'},$$

and the formula

$$\sum_{m=-n}^{n} Y_{n,m}^*(\mu, \phi)Y_{n,m}(1, 0) = \frac{2n + 1}{4\pi}P_n(\mu),$$ (9)

where P_n is the nth-order Legendre polynomial, we arrive at the frequency-dependent ACF

$$\rho_\omega(\cos\theta) = \rho_\omega(\mu) = \frac{C_\omega(\mu)}{C_\omega(1)},$$

where

$$C_\omega(\mu) \equiv \frac{\sigma^2}{4\pi}\sum_{n=0}^{\infty} \frac{(2n + 1)P_n(\mu)}{\omega^2\tau_r^2 + [\lambda^2 n(n + 1) + 1]^2}.$$ (10)

The frequency-dependent ACF $\rho_\omega(\cos\theta)$ is plotted for $\lambda = 0.4$ and $\lambda = 0.2$ and for different values of $\omega\tau_r$ in Fig. 1. We observe that it approaches a limit function $\rho_0(\cos\theta)$ as $\omega\tau_r \rightarrow 0$. The instantaneous spatial covariance is computed in appendix B [Eq. (B2)] to yield

$$C(\mu) = E[T(t, \mu, \phi)T^*(t, 1, 0)]$$
$$= \frac{1}{2\pi}\int_{-\infty}^{\infty} C_\omega(\mu)\, d\omega.$$ (11)

Equation (11) is also derived for a more general EBM at the end of section 3a. The integral diverges in the limit $\mu \rightarrow 1$ ($\theta \rightarrow 0$). This is because the diffusion operator is unable to smoothen the irregularities introduced by the
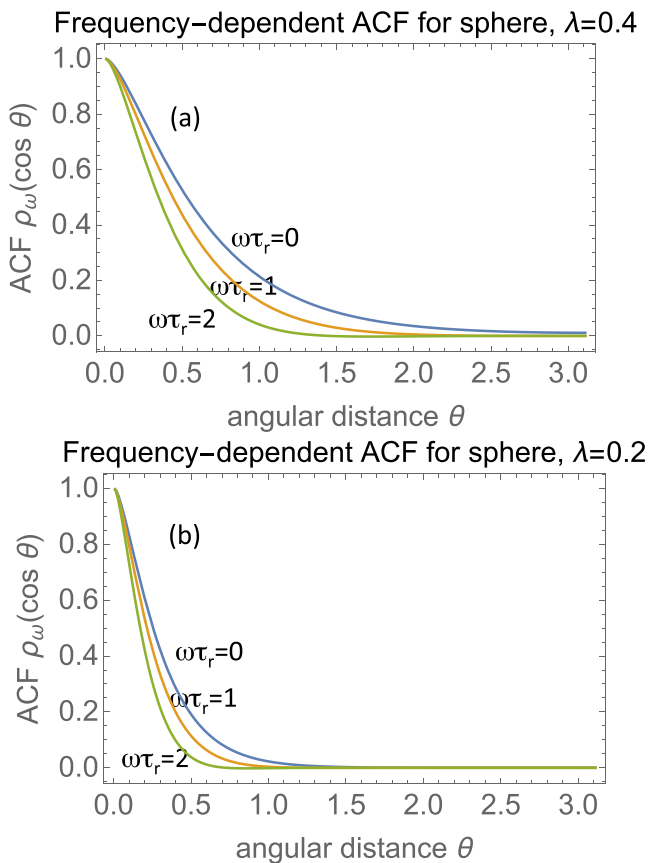
FIG. 1. Frequency-dependent spatial ACF of temperature measured vs angular distance θ from any reference point on the uniform unit sphere given by Eq. (10) for (a) $\lambda = 0.4$ and (b) $\lambda = 0.2$.

FIG. 2. (a): Instantaneous spatial covariance, $C_{\omega_K}(\cos\theta)$, as computed from Eq. (B2) for $\sigma^2 = 1$, $\lambda = 0.2$ and three different values of the Nyquist frequency ω_K. Blue curve: $\omega_K\tau_r = 1$, orange curve: $\omega_K\tau_r = 10$, green curve: $\omega_K\tau_r = 100$, dashed curve: $122 \times C(\cos\theta)$, where $C(\mu)$ is given by Eq. (B6). (b) The corresponding ACFs defined as $\rho_{\omega_K} = C_{\omega_K}(\cos\theta)/C_{\omega_K}(1)$.

random forcing field on the shortest time scales. This irregularity vanishes if we truncate the Fourier expansion in time at a finite K (i.e., if we assume that the forcing field is smooth on time scales shorter than $1/\omega_K$). In Fig. 2a we have plotted the truncated $C_{\omega_K}(\mu)$ given in Eq. (B2) for $\lambda = 0.2$ for three different values of the upper (Nyquist) frequency. We note that $C_{\omega_K}(\mu)$ converges to a finite $C(\mu)$ except for $\mu = 1$. However, because $C_{\omega_K}(1)$ diverges, the decorrelation time of the truncated ACF, $\rho_{\omega_K}(\mu) = C_{\omega_K}(\mu)/C_{\omega_K}(1)$, goes to zero as $\omega_K \to \infty$, as shown in Fig. 2b. In appendix B we also compute an ordinary differential equation for the instantaneous spatial ACF, $C(\mu)$. The solution is given in terms of the Legendre function, $Q_n(\mu)$, which in general diverges at $\mu = 1$. This solution is plotted as the dashed curve in Fig. 2a. The importance of Fig. 2 is to be aware that the instantaneous ACF computed from observation data will depend on the sampling rate of the data analyzed, while the frequency-dependent ACFs will not.

From putting $\hat{\mathbf{r}} = \hat{\mathbf{z}}$ in Eq. (8) we observe that $C_\omega(1) = E[|T(\omega, 1, 0)|^2]$ is the temporal PSD of the temperature time series at any point on the sphere. If we
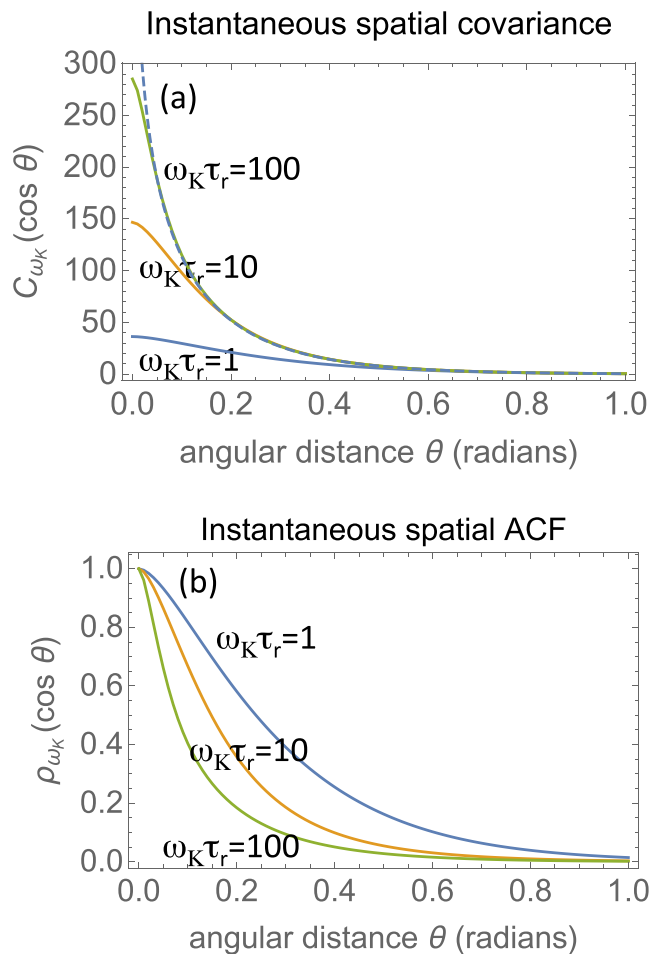
set $\mu = 1$ in Eq. (10), and use that $P_n(1) = 1$ for all $n = 1, 2, \ldots$, we find

$$S(\omega) = C_\omega(1) = \frac{\sigma^2}{4\pi} \sum_{n=0}^{\infty} \frac{(2n+1)}{\omega^2\tau_r^2 + [\lambda^2 n(n+1) + 1]^2}. \quad (12)$$

The PSD $S(\omega)$ is plotted in Fig. 3 for different values of λ. Note that since we operate on the unit sphere λ is measured in radians. For time scales longer than the relaxation time τ_r ($\omega\tau_r < 1$), the spectrum is flat, which indicates that there is no memory on those time scales. According to North et al. (2011) τ_r is a few months over land, and several years over oceans. By estimating τ_r for the corresponding zero-dimensional model (a model for global temperature), Rypdal and Rypdal (2014) found $\tau_r = 4.7$ yr. The flat spectrum for longer time scales than this is not consistent with spectra obtained from instrumental data records over oceans, where we find power-law spectra with $\beta \approx 1$ on time
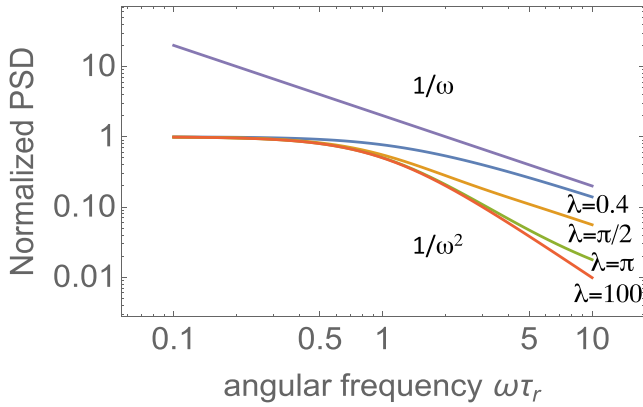
FIG. 3. Log–log plots of the temporal PSD of temperature time series at any point on the uniform unit sphere given by Eq. (9), for $\lambda = 0.4$, $\pi/2$, π, 100. For $\omega\tau_r \gg 1$ the slope corresponds to $\beta \approx 1$ for $\lambda \ll \pi$ and to $\beta \approx 2$ for $\lambda \gg \pi$.

scales up to a decade. In section 4 we shall demonstrate that such power-law spectra also extend to century time scales in the NorESM model.

b. Relating temporal and spatial correlations

A major objective of the present paper is to relate the temporal correlation structure in regionally, hemispheric or globally averaged temperature to the local temporal correlations and the spatial, frequency-dependent correlations. We start by defining a spatially averaged temperature over a region (solid angle) Ω on the unit sphere,

$$T_\Omega(t) = \frac{1}{\Omega} \int_\Omega T(\theta, \phi, t) \, d\phi \sin\theta \, d\theta.$$

We make the Fourier transform of this integral in time and then form the temporal PSD,

$$\begin{aligned}
S_\Omega(\omega) &= \frac{1}{\Omega^2} E[T_{\Omega,\omega} T_{\Omega,\omega}^*] \\
&= \frac{1}{\Omega^2} \int_\Omega d\phi' \sin\theta' \, d\theta' \int_\Omega C_\omega(\cos\theta) \, d\phi \sin\theta \, d\theta \\
&= \frac{1}{\Omega} \int_\Omega C_\omega(\cos\theta) \, d\phi \sin\theta \, d\theta \\
&= \frac{S(\omega)}{\Omega} \int_\Omega \rho_\omega(\mu) \, d\phi \, d\mu.
\end{aligned}$$

Here we have used the (unrealistic) assumption that

$$E[T_\omega(\hat{\mathbf{r}}) T_\omega^*(\hat{\mathbf{r}}')] = C_\omega(\cos\theta) = C_\omega(\mu) \quad (13)$$

depends only on the angular distance θ between two points on the sphere. If Ω is the solid angle of a spherical cap characterized by $\mu_0 = \cos\theta_0$ this reduces to

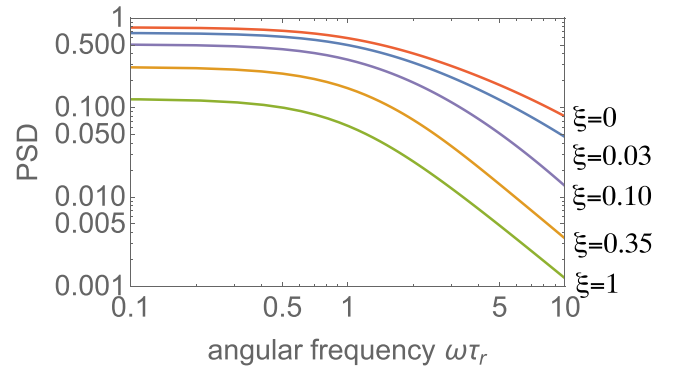$$S_{\mu_0}(\omega) = S(\omega) \frac{1}{1 - \mu_0} \int_{\mu_0}^1 \rho_\omega(\mu) \, d\mu. \quad (14)$$

FIG. 4. Log–log plot of power spectral density for the temperature averaged over a fractional area $\xi = A/4\pi = (1 - \cos\theta)/2$ of the unit sphere as given by Eq. (14), for $\xi = 0$, 0.03, 0.1, 0, 35, 1. The slope for $\omega\tau_r \gg 1$ and $\xi = 0$ approaches $\beta = 1$. For $\xi = 1$ (global average) we have $\beta = 2$.

If Ω is the entire sphere, then $\mu_0 = -1$ and $S_{-1}(\omega)$ is the PSD of the global temperature. The interesting feature of Eq. (14) is that it expresses the PSD of the regional or global temperature as a product of the local PSD, $S(\omega)$, and a spatial integral over the frequency-dependent spatial ACF, $\rho_\omega(\mu)$. It is generally valid for any statistically uniform field [satisfying Eq. (13)] on a sphere, and not just for solutions of the North EBM. For the EBM we saw in Fig. 1 that $\rho_\omega(\mu) \to \rho_0(\mu)$ as $\omega\tau_r \to 0$. This means that for $\omega\tau_r \ll 1$ we have that $S_{-1}(\omega) \propto S(\omega)$; that is, the PSD of the global temperature scales the same way as the local temperature for frequencies lower than the inverse time constant. However, for $\omega\tau_r > 1$, the integral $\int_{-1}^1 \rho_\omega(\mu) \, d\mu$ varies with frequency and hence explains the different scaling exponent β for local and global temperature observed in Fig. 4. Equation (14) shows that in general, if $\rho_\omega(\mu)$ for a statistically uniform field on a sphere approaches a limit function $\rho_0(\mu)$ for $1/\omega$ greater than a certain time scale τ, then local and global temperature should scale the same way for all time scales greater than τ. In the NorESM data we are not able to identify such a time scale τ (i.e., if it exists it must be more than several centuries). This is a major motivation for searching for a generalization of the North EBM, which does not exhibit the same scaling for local and global time series at low frequencies.

3. Generalizations of the North EBM

a. Transfer function formulation

The Fourier representation (in time) of Eq. (2) given by Eq. (7) is expressed through the transfer functions

$$g_n(\omega) = \frac{1}{(-i\omega\tau_r + 1) + \lambda^2 n(n+1)}, \quad (15)$$

such that

$$T(\omega, \mu, \phi) = \sum_{n=0}^{\infty} g_n(\omega) \sum_{m=-n}^{n} F(\omega, n, m) Y_{n,m}(\mu, \phi). \quad (16)$$

In the following we will specify a choice of the sequence $\{g_n(\omega)\}$ that corresponds naturally to the generalization from a zero-dimensional EBM with an exponential relaxation time to a zero-dimensional EBM with a long-memory response, but first we will point out some results that are independent of the choice of functions $g_n(\omega)$. The general form of Eq. (10) is

$$C_\omega(\mu) = \frac{\sigma^2}{4\pi} \sum_{n=0}^{\infty} |g_n(\omega)|^2 (2n+1) P_n(\mu). \quad (17)$$

If we take the inverse Fourier transform (in time) of Eq. (16) we obtain the expression

$$T(t, \mu, \phi) = \sum_{n=0}^{\infty} \sum_{m=-n}^{n} Y_{n,m}(\mu, \phi) \int g_n(\omega) F(\omega, n, m) e^{-i\omega t} \, d\omega,$$

and if the forcing is white noise (in time and space) we have

$$E\left[\int g_n(\omega) F(\omega, n, m) e^{-i\omega t} \, d\omega \right] \left[\int g_{n'}(\omega) F(\omega, n', m') e^{-i\omega t} \, d\omega \right]^*$$
$$= \sigma^2 \int |g_n(\omega)|^2 \, d\omega \delta_{n,n'} \delta_{m,m'},$$

and using this, we easily recover that Eq. (11) is valid for any response function. The more cumbersome derivation in appendix B serves to demonstrate why $C(\mu)$ diverges for $\mu = 1$ and how to understand the instantaneous spatial ACF.

b. The fractional EBM

The response in global surface temperature can be found by integrating the model over the sphere, or equivalently letting $\lambda = 0$ (note that this is very different from the limit $\lambda \to 0$; a spatiotemporal model with vanishing diffusion coefficient). The first term in the denominator in Eq. (15) is $-i\omega\tau_r + 1$, and we note that

$$G_0(\omega) = \frac{1}{-i\omega\tau_r + 1}$$

is the transfer function corresponding to the differential operator $\tau_r \partial_t + 1$ (i.e., of the zero-dimensional EBM). Hence the transfer functions $g_n(\omega)$ can be written in the form

$$g_n(\omega) = \frac{1}{G_0^{-1}(\omega) + \lambda^2 n(n+1)}. \quad (18)$$

The inverse Fourier transform of $G_0(\omega)$ is an exponential function with time constant τ_r; that is, the Green's function for the zero-dimensional EBM is

$$G_0(t) = \frac{2\pi}{\tau_r} e^{-t/\tau_r} \Theta(t),$$

where $\Theta(t)$ is the unit step function. This is the response in the global surface temperature to a delta function $\delta(t)$ in the forcing. The generalization suggested in Rypdal (2012) and Rypdal and Rypdal (2014) is to replace the exponentially decaying response function by a power-law function

$$G(t) = (t/\eta)^{\beta/2 - 1} \xi \Theta(t), \quad (19)$$

which is equivalent to the fractional differential equation

$$\frac{c}{2\pi} D_t^{\beta/2} T(t) = F(t),$$

with

$$c = \frac{2\pi \eta^{\beta/2 - 1}}{\xi \Gamma(\beta/2)},$$

where Γ is the Euler gamma function and η is a constant parameter of dimension time that characterizes the strength of the response. The unit constant $\xi = 1$ has dimension $(\text{time})^{-1}$. The Fourier transform of $G(t)$ is

$$G(\omega) = \frac{1}{2\pi} e^{i\pi\beta \text{sgn}(\omega)/4} \Gamma(\beta/2) \xi \eta |\eta\omega|^{-\beta/2}, \quad (20)$$

and the corresponding modification of the North EBM is the replacement $G_0(\omega) \to G(\omega)$ in Eq. (18), that is,

$$g_n(\omega) = \frac{1}{c e^{-i\pi\beta \text{sgn}(\omega)/4} |\omega|^{\beta/2} + \lambda^2 n(n+1)}. \quad (21)$$

The constant c has dimension $(\text{time})^{\beta/2}$, hence $c^{2/\beta}\omega$ is a dimensionless frequency. Note that the solution $T(\omega, \mu, \phi)$ obtained in Eq. (16) is the solution of the equation

$$e^{-i\pi\beta \text{sgn}(\omega)/4} |c^{2/\beta}\omega|^{\beta/2} T - \lambda^2 \nabla^2 T = F, \quad (22)$$

where ∇^2 is the dimensionless Laplace operator on the unit sphere. The first term on the left can be considered as the Fourier transform of a fractional time derivative (Rypdal 2012). In the time domain this equation can be written as

$$\frac{c}{2\pi}D_t^{\beta/2}T - \lambda^2\nabla^2 T = F,$$

which is why we call this equation a fractional EBM. In the present context, however, the formalism of fractional derivatives has no practical use, the temperature response is computed by the inverse Fourier transform of Eq. (16), using the transfer functions Eq. (21). Figure 5 shows a snapshot of such a solution computed for a simulated random force field.

c. Spatial and temporal correlations in the fractional EBM

From Eq. (21) we have

$$|g_n(\omega)|^2 = \frac{1}{|c^{2/\beta}\omega|^\beta + [\lambda^2 n(n+1)]^2 + 2\lambda^2 n(n+1)|c^{2/\beta}\omega|^{\beta/2}\cos\left(\frac{\pi\beta}{4}\right)}, \qquad (23)$$

which we can insert into Eq. (17) to obtain explicit expressions for $C_\mu(\omega)$ and $S(\omega) = C_1(\omega)$.

The frequency-dependent ACF is plotted in Fig. 6 for two values of λ and is the analog of Fig. 1 generalized to the fractional EBM. We have the same tendency toward loss of long-range spatial correlation at high frequencies, but in the zero frequency limit the correlation function is uniform; that is, the fluctuations are dominated by spatially uniform (global) variations. Such behavior does not appear in the conventional EBM since that model lacks a long-range global response reflecting the slow response of the deep ocean.

In Fig. 7 we plot the PSD of the local temperature for a number of different λ values. This figure is the fractional analog of Fig. 3. For small and large λ these spectra are perfect power laws over most of the frequency range. For small λ (i.e., in the regime relevant for the Earth climate system) the spectral exponent is $\beta/2$ (i.e., half of the spectral exponent for the global temperature in the zero-dimensional fractional model; Rypdal and Rypdal 2014). For $\lambda \gg \pi$, the spectrum is a power law with spectral exponent β. This result is obvious, since in the large λ limit the field will be spatially uniform and the model reduces to the zero-dimensional one. For intermediate values of λ there is a break in the scaling from exponent β at low frequencies (dominated by global fluctuations) to $\beta/2$ at high frequencies (dominated by local fluctuations).

We can also compute the PSD for the temperature averaged over a fraction ξ of the globe surface, as we did in Fig. 4 for the conventional EBM. The result is shown in Fig. 8. It may not come as a surprise that the spectra are power laws, and that local spectra have exponent $\beta/2$, gradually increasing to β with increasing degree of spatial averaging up to global.

In Fig. 9 we show that this feature is also reflected in observation data. The figure shows the fluctuation functions of a first-order detrended analysis (DFA1) (Kantelhardt et al. 2001) of the central England instrumental temperature record and two globally averaged records. DFA1 does not eliminate linear trends, but this trend is small in the 350-yr-long central England record. The averaged records are derived from the 160-yr-long HadCRUT3 global instrumental surface temperature (Brohan et al. 2006) and the 2000-yr-long Northern Hemisphere reconstruction of Moberg et al. (2005). The scaling properties of these records may be strongly influenced by the global radiative forcing and hence not representative of the internal (unforced) variability. However, by using a reconstruction of the forcing (Hansen et al. 2011; Crowley 2000) and a model for the global temperature response we can compute the temperature response to this deterministic forcing. This was done by Rypdal and Rypdal (2014), who also demonstrated that a simple zero-dimensional, fractional EBM response model yields a deterministic response almost indistinguishable from the mean response in ensembles of CMIP5 model runs. The residual noise obtained by subtracting the deterministic response from the observed/reconstructed record represents the internal variability, and it is these records that have been subject to analysis in Fig. 9. The slope α of the fluctuation-function curve is related to the spectral exponent β via $\alpha = (1 + \beta)/2$, and the slopes correspond to $\beta \approx 0.4$ for the local central England record, and to $\beta \approx 0.8$ for the global-scale records, in agreement with the fractional EBM result that the global β is twice the local β.

4. Comparison to NorESM data

The simple version of the North EBM and the fractional EBM we have explored here assumes a uniform Earth surface. Since the global spatial average of these models are identical to the zero-dimensional "exponential" and "scale-invariant" response models studied in Rypdal and Rypdal (2014), we can use their methods for estimating the model parameters τ_r (for the North EBM) and β and η (for the fractional EBM). The temperature data records to
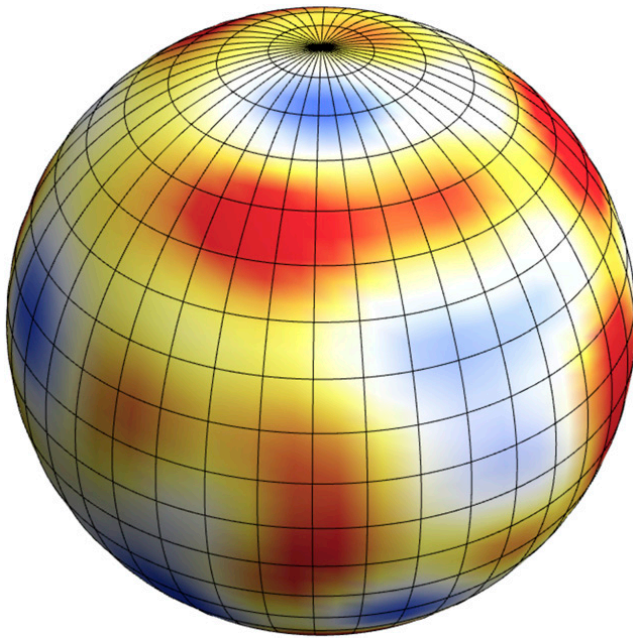
FIG. 5. Instantaneous temperature field in a simulation of the fractional EBM on a sphere. The parameters are $\beta = 0.75$ and $\lambda = 0.4$, which are typical for an ocean planet.

use as input for such estimates can be the instrumental record for global land temperature or sea surface temperature, depending on whether we want to study spatiotemporal persistence over continental interiors or over oceans.

As discussed in the previous section, the β for unforced dynamics should be estimated from the residual obtained by subtracting the deterministic response from the observed record. In Figs. 10a and 11a the red full curve is the deterministic solution to the fractional EBM when $\beta \approx 0.61$ is estimated from the full record. The estimation method used here is to model the full record as a fractional Gaussian noise (fGn) and determine the β of that fGn that minimizes the mean square error. If we subtract the red full curve from the observed record and estimate β again from the residual record, we find $\beta = 0.28$. The deterministic response with this new β is the dotted red curve, which is almost the same. Hence in the fractional EBM the response to the deterministic forcing is not very sensitive to β, and hence that $\beta = 0.28$ self-consistently describes the unforced dynamics. The situation is different for the North EBM for which results are shown in Fig. 10b. Here the time constant is $\tau_r \approx 8.0$ yr estimated from the full record and $\tau_r \approx 1.7$ yr from the residual, and the corresponding deterministic responses are quite different. The response to the deterministic forcing is better described by the large τ, but the random fluctuations requires a shorter response time, and suggests that the response is characterized by more than one time constant, as in the two-layer model considered by Geoffroy et al. (2013).
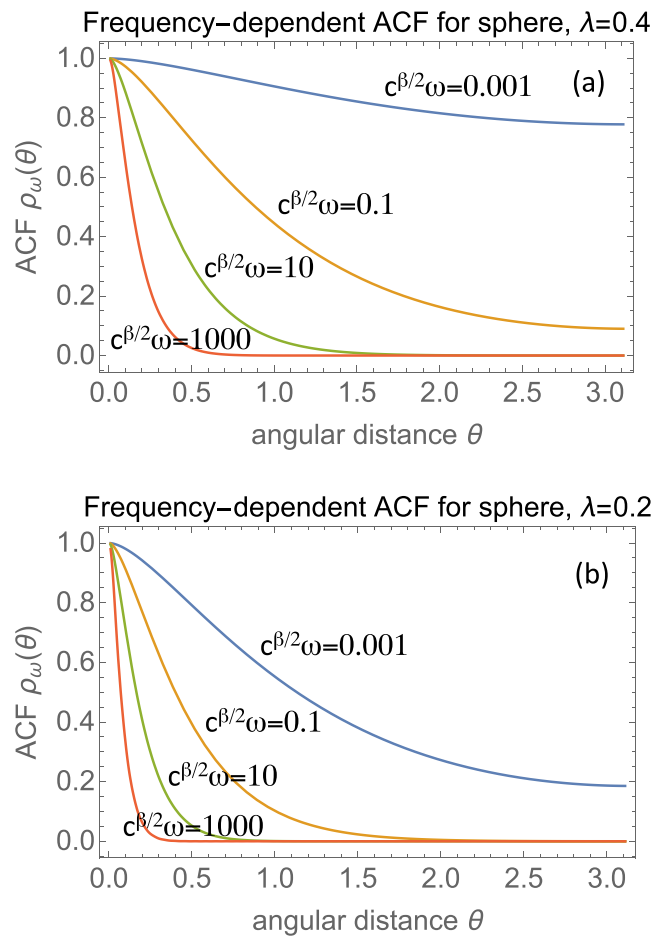

FIG. 6. Frequency-dependent spatial ACF of temperature measured vs angular distance θ from any reference point on the uniform unit sphere given by Eqs. (17) and (23) for (a) $\lambda = 0.4$ and (b) $\lambda = 0.2$.

Similar observations are made for the ocean temperatures as shown in Figs. 11a and 11b.

The diffusion parameter λ cannot be estimated from such globally averaged records, so these must be obtained
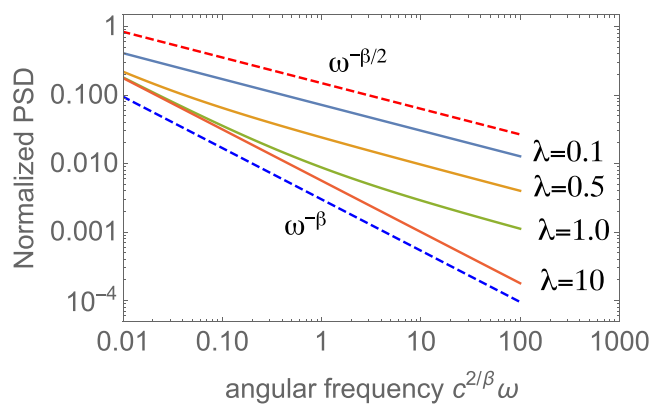

FIG. 7. Log–log plots of the temporal PSD of temperature time series at any point on the uniform unit sphere given by Eq. (17) for $\lambda = 0.1, 0.5, 1.0, 10$. The blue dashed line has slope $-\beta$, and the red dashed line has slope $-\beta/2$.
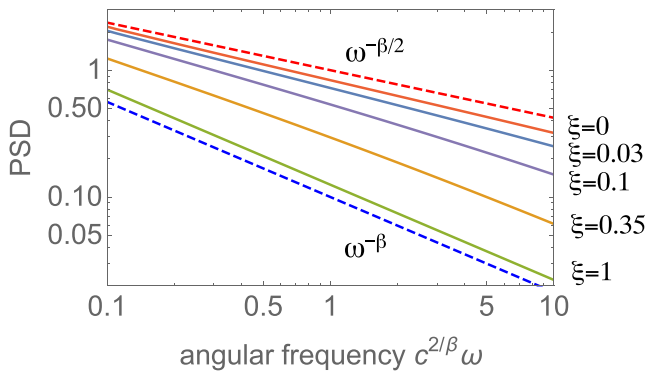
FIG. 8. Log–log plot of power spectral density for the temperature averaged over a fractional area $\xi = A/4\pi = (1 - \cos\theta)/2$ of the unit sphere as given by Eq. (14) and $S(\omega)$ and $\rho_\omega(\mu)$ computed from the fractional EBM, for $\xi = 0, 0.03, 0.1, 0, 35, 1$.

from spatiotemporal observation data, reanalysis data, or data from AOGCMs. The latter provide the best data coverage in space and longer temporal records, which make it possible to "calibrate" the EBMs to general circulation models. For this purpose we use the frequency-dependent ACF $\rho_\omega(x)$ computed from the surface temperature field derived from long control runs of the NorESM [see Bentsen et al. (2013) and Iversen et al. (2013) for general descriptions of the NorESM1-M model]. Such ACFs are shown for Eurasian land temperature as the pointed curves in Fig. 10c. Each curve corresponds to a given frequency $\omega = 2\pi f$, where the highest frequency is $f_1 = 1\ \mathrm{yr}^{-1}$ and the other frequencies are $f_2 = f_1/3$, $f_3 = f_1/10$, $f_4 = f_1/30$, and $f_5 = f_1/100$. This corresponds to periods $1/f$ of 1, 3, 10, 30, and 100 yr. There seems to be a weak elevation of the ACF for $x \sim 4000\ \mathrm{km}$ for all these frequencies, and a strong elevation for periods approaching 100 yr. The former may be the characteristic spatial extent of modes of interannual and decadal variability, while the latter may reflect the spatial structure of a multidecadal oscillation. These modes are of course not represented in the EBMs.

The next step is to compute $\rho_\omega(x)$ from the fractional EBM with the parameters β and η estimated from the observed global land temperature and different λ and select the value of λ that minimizes the mean square error between the theoretical and observed ACFs in the range $0 < x < 4000\ \mathrm{km}$. The resulting ACFs computed from the fractional EBM with the estimated model parameters, and for the same frequencies as above, are shown as the full curves in Fig. 10c. Because of the multidecadal oscillation the correlation structure is poorly described by the model for distances longer than 4000 km, but otherwise the ACFs of the model has similar shapes and the same tendency toward increasing width as periods are increased.

In Fig. 10d we show similar results for the North EBM, where the time constant τ_r estimated from the global land temperature record has the very low value $\tau_r \approx 1.7$ yr.
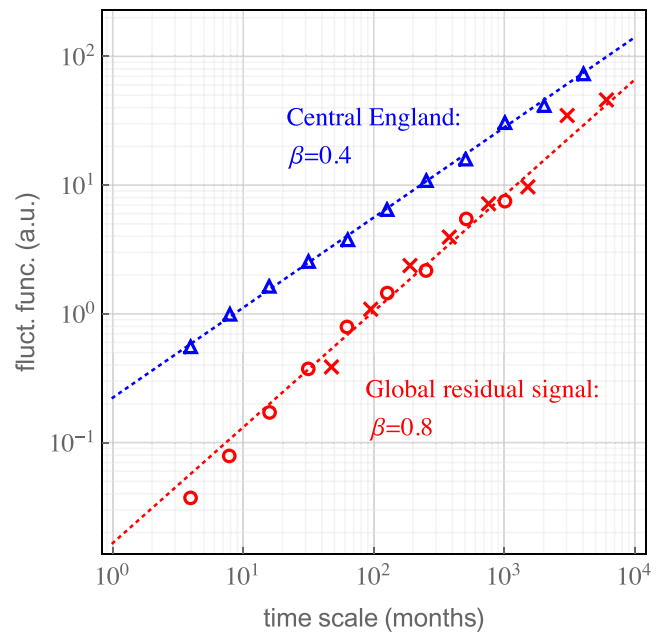

FIG. 9. DFA1 fluctuation functions of the temperature record for central England (blue triangles), Moberg's reconstruction of the mean surface temperature in the Northern Hemisphere in the last millennium (red crosses), and the instrumental record for global mean temperature (red circles). For the global data the records analyzed are the residuals after the response to the deterministic forcing has been subtracted. The blue dotted line corresponds to $\beta \approx 0.4$ and the red dotted line corresponds to a $\beta \approx 0.8$.

In this model the width of the ACF does not increase gradually with increasing period, as in the AOGCM data and the fractional EBM. It rather converges to the zero-frequency limit $\rho_0(x)$, and is close to this limit already for periods greater than 3 yr. For periods less than a decade the model predicts much smaller correlation lengths than observed in the NorESM model. Hence these results show that for land data the fractional EBM provides a much more accurate description than the North EBM.

Corresponding results for ocean temperatures are shown in Fig. 11. To avoid a strong influence from El Niño–Southern Oscillation in the ACF on interannual time scales we study only the oceans south of 20°S in the NorESM control run. We obtain $\beta \approx 0.77$ from the residual record, which is close to what we found for the global observed temperature in Fig. 9. For these data the fractional EBM produces ACFs that fit better to the ACFs from the NorESM model for periods less than a decade, but not for longer time scales. The reason for this poor performance of the fractional model for oceans will become clear in the forthcoming section, where we propose a modification of the model based on data from NorESM simulations with instantaneous (step function) increase in CO_2 forcing.

The performance of the two EBM models with respect to reproducing the observed global-scale PSDs is shown in Fig. 12. The black curves are the spatially averaged spectra
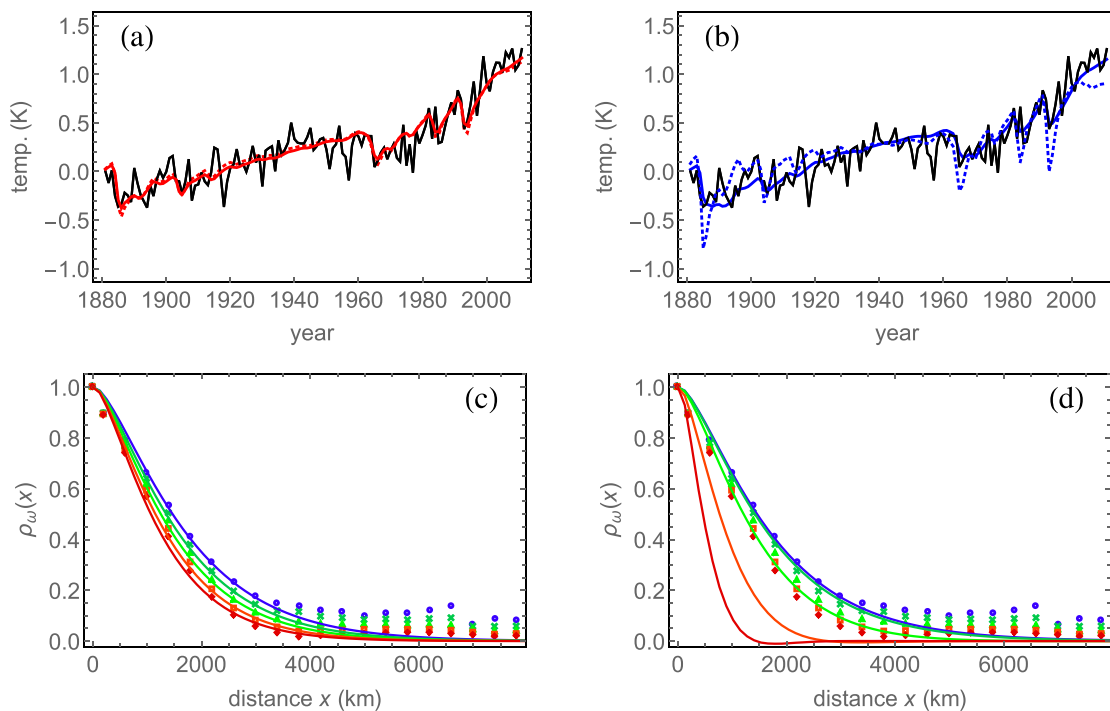
FIG. 10. (a) The black curve is the global mean land surface temperature. The red solid curve is the mean temperature in the fractional EBM with deterministic forcing and parameters estimated using the least squares method. The estimated β value is 0.61. The red dotted curve is the same as the red solid curve, but in this case the β parameter is estimated from the residual signal obtained by taking the difference between the temperature observations (black curve) and the least squares fit (solid red curve). This β value is 0.28. (b) As in (a), but in this case for the North EBM. The solid blue line shows the response to the deterministic forcing with parameters estimated using the least squares method. This gives the estimate $\tau_r = 8.0$ yr. The blue dotted curve is constructed by estimating the response time from the residual signal. This gives $\tau_r = 1.7$ yr. (c) The solid curves are the spatial ACFs given by Eqs. (17) and (23), and the points are the corresponding estimates obtained from the land surface temperatures over the Eurasian continent in a NorESM control run. The frequencies chosen are $1/100$ yr^{-1} (blue), $1/30$ yr^{-1} (dark green), $1/10$ yr^{-1} (light green), $1/3$ yr^{-1} (light red), and 1 yr^{-1} (dark red). We estimated $\lambda = 0.275$ by fitting the spatial ACF to the NorESM data on the lowest frequency ($1/100$ yr^{-1}) on distances up to 2500 km. The parameters $\beta = 0.28$ and $c = 8.7$ are estimated from the global response to the deterministic forcing as shown in (a). (d) As in (c), but for the North EBM; i.e., the solid curves are given by Eqs. (17) and (15). The parameters are $\lambda = 0.18$ and $\tau_r = 1.7$ yr.

of local temperatures over the Eurasian continent (Fig. 12a) and over the Southern Ocean (Fig. 12b). The red curves are the theoretical spectra from the fractional EBM and the blue curves for the North EBM, demonstrating very clearly the superiority of the fractional model.

5. Fractional forcing noise

From Figs. 10c and 11c we have observed that the fractional EBM provides a less accurate description of the correlation structure for sea surface temperatures as compared to the land temperatures. However, the comparison with the NorESM model improves significantly if we allow the stochastic forcing F to be an fGn with an exponent $\beta_f > 0$ rather than the white noise ($\beta_f = 0$) considered so far. If the average temperature of the Southern ocean in the NorESM control run can be modeled by a fractional EBM characterized by a response exponent β, and this EBM is driven by an fGn with

spectral exponent β_f, then the global-scale temperature of the control run is a realization of an fGn with spectral exponent $\beta_{cr} = \beta + \beta_f$.

Such a generalization of the fractional EBM would be rather ad hoc if it was not directly suggested by other climate model simulations. Geoffroy et al. (2013) studied a large number of such runs of CMIP5 models, with results that were all similar to the black curve in Fig. 13a, which is the global temperature following sudden quadrupling of atmospheric CO_2 concentration in the NorESM model. Geoffroy et al. (2013) find good fits to these curves with a function that is a linear combination of two exponential functions with one small time constant of the order of a few years and one larger of the order of a century. In Fig. 13a the red curve is a fit of a power-law function $t^{\beta/2}$, with $\beta = 0.36$. On the shorter time scales (up to few years) the fit is not good, because a power law with $\beta < 1$ has a diverging derivative as $t \to 0$, which is not physical. But our interest in the power-law response
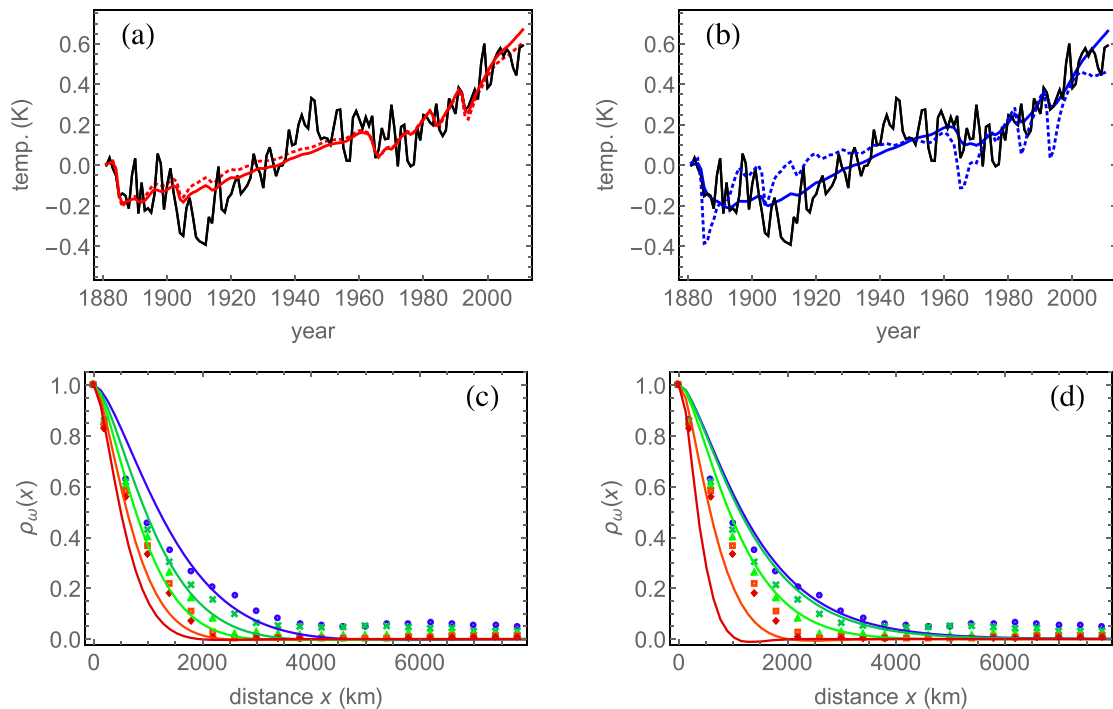
FIG. 11. As in Fig. 10, but for sea surface temperatures. (a) The estimated scaling exponent is $\beta = 1.03$. The dotted red line is the response to the deterministic forcing with the parameter $\beta = 0.77$ obtained from the residual signal. (b) The estimate is $\tau_r = 20.4$ yr. The blue dotted curve is constructed by estimating the response time from the residual signal. This gives $\tau_r = 2.0$ yr. (c) As in Fig. 10, the solid curves are the spatial ACFs, and the points are the corresponding estimates obtained from the sea surface temperatures for the region south of 20°S in a NorESM control run. The frequencies chosen are the same as in Fig. 10. We estimated $\lambda = 0.68$ by fitting the spatial ACF to the NorESM data on the lowest frequency ($1/100$ yr^{-1}). The parameters $\beta = 0.77$ and $c = 63.6$ are estimated from the global response to the deterministic forcing as shown in (a). (d) As in (c), but for the North EBM. The parameters are $\lambda = 0.15$ and $\tau_r = 2.0$ yr.

function is as a model for the response on time scales from decades to centuries, for which it seem to perform quite well. In this respect, these climate model runs support the fractional EBM as a model for the global response. We observe, however, that the estimated β for the response is roughly half the value of β_{cr} estimated from global temperature [or average Southern Ocean (SO) temperature] in control runs. This discrepancy is explained if we assume a fractional forcing such that $\beta_f = \beta_{cr} - \beta$. Recall that an estimate of β_{cr} can be obtained from the spatially averaged SO temperature in the control run, and β from the transient evolution shown in Fig. 13a. Hence we have $\beta_f = \beta_{cr} - \beta \approx 0.77 - 0.36 = 0.41$. The deterministic response corresponding to $\beta = 0.36$ is given by the red curve in Fig. 12b, and Fig. 12c shows the frequency-dependent ACFs computed from this generalized, fractional EBM. The expressions for these ACFs are slightly modified from the original fractional EBM, and are given in appendix C [Eq. (C2)]. There we also show that the *local* spectrum for the generalized, fractional EBM has exponent $\beta_f + \beta/2$. The ACFs of the fractional EBM are now much closer to those of the SO in the NorESM. In Fig. 13d the lower black curve is the

spectrum of the averaged SO temperature and the red line the power-law spectrum with the estimated exponent β_{cr}, hence the red line represents a fit to the spectrum. The upper black curve is the average of the *local* spectra of the SO. Here the red line is the power-law spectrum with exponent $\beta_f + \beta/2 \approx 0.59$, where $\beta_f \approx 0.41$ and $\beta \approx 0.36$ have been estimated as described above. Hence, this line is not a fit to the observed spectrum but a result of the generalized fractional EBM. The fact that the fit is good confirms the consistency between this model and the NorESM data.

6. Conclusions

In an editorial comment, Mann (2011) asserted that the scaling behavior in instrumental and long-term proxy temperature reconstructions appears consistent with the results of a standard, zero-dimensional EBM forced by estimated natural and anthropogenic radiative forcing changes, and subject to white-noise stochastic weather forcing. According to this author, "nothing more exotic than the physics of such a simple model is necessary to explain the apparent scaling behavior in observed surface
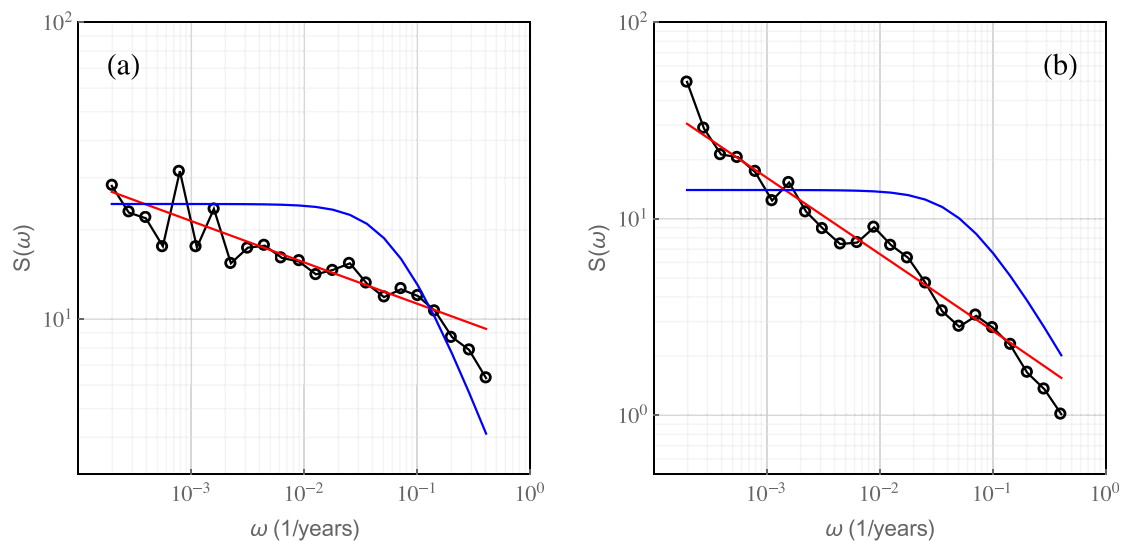
FIG. 12. (a) The black circles show the average power spectral density for the temperatures on the Eurasian continent in a control run of the NorESM model. The blue curve is the power spectral density for local temperatures in the North EBM [Eq. (12)] with parameters $\tau_r = 1.73$ and $\lambda = 0.18$. The red curve is the power spectral density for local temperatures in the fractional EBM [Eqs. (17) and (23)] with parameters $\beta = 0.28$ and $\lambda = 0.44$. (b) As in (a), but for ocean temperatures. The black circles show the average power spectral density for the temperatures in sea surface south of 20°S in a control run of the NorESM model. The blue curve is the power spectral density for local temperatures in the North EBM with parameters $\tau_r = 2.0$ and $\lambda = 0.15$. The red curve is the power spectral density for local temperatures in the fractional EBM with parameters $\beta = 0.77$ and $\lambda = 0.51$.

temperatures.'' This conclusion was drawn from application of a number of standard estimation techniques for β to realizations of the purely stochastically forced, and stochastic plus radiatively forced, EBM. These estimates were compared to results from the same techniques applied to observation data. Such comparisons show overlap of the distributions of β estimates for the model realizations and the observation records, which lead the author to conclude that the scaling properties of the observation data are consistent with this simple model.

The results derived in the present paper demonstrate that there is a clear discrepancy between the scaling properties of the North EBM and data derived from observations and climate models. The conclusions of Mann (2011) arise from uncritical application of estimation techniques for the scaling exponent to time series that do not exhibit scaling. For instance, the stochastically forced model signal is an AR(1) process, which scales like a Wiener process ($\beta = 2$) on scales shorter than the autocorrelation time and as a white noise ($\beta = 0$) on longer time scales. There is no unique scaling exponent for this process. Careful examination of power spectra or fluctuation functions for model data and observation data, in particular of the residual resulting from subtracting the (deterministic) radiatively forced response from the observations, demonstrates very clearly that the spatiotemporal scaling properties of the North EBM data are different from those of the observation data. We also demonstrate that the model can produce the observed

scaling by a generalization which involves a long-range memory response that can be interpreted as a delayed heat exchange between the ocean mixed layer and the deep ocean. This physics goes beyond the simple "one-box" energy balance model, but it is not particularly "exotic."

The fractional EBM not only explains the power-law temporal scaling, but also how and why the spectral exponent increases with increased spatial averaging, and it describes the main features of the frequency-dependent spatial autocorrelation functions. An inconsistency between the standard fractional EBM and climate models simulations is observed in the transient response to sudden change in forcing, giving a lower β for the response than observed in the control runs. The consistency is restored by assuming that the stochastic forcing is a fractional noise with $\beta \approx 0.4$. One can think of this forcing as exchange of sensible and latent heat between the atmosphere and land surface/ocean mixed layer influenced by atmospheric weather systems, but radiative forcing, such as the CO_2 greenhouse effect, also has a noisy component that may exhibit long-range persistence. This assertion is supported by recent direct observations of CO_2 forcing at Earth's surface. Feldman et al. (2015) measured the clear-sky radiative CO_2 surface forcing and obtained time series as shown in Fig. 14a. The PSD of this time series has a spectral exponent $\beta \approx 2$ (Fig. 14b), but this value is determined by the strong anthropogenic trend. There is also a strong seasonal trend that appears as peaks at the first and
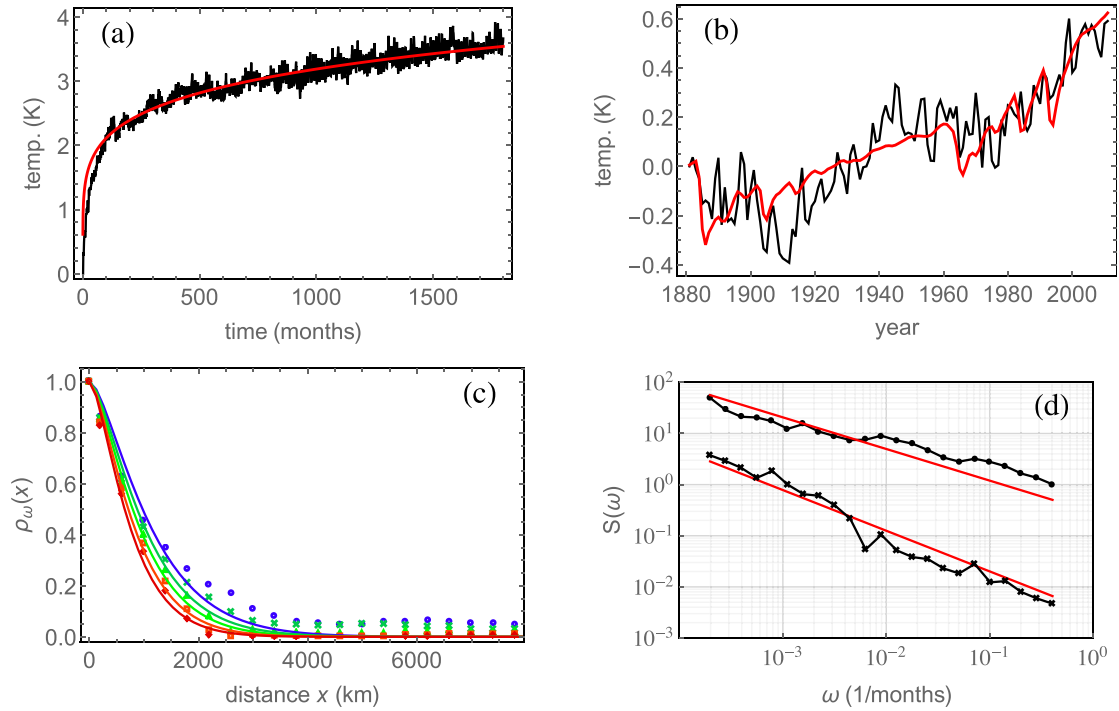
FIG. 13. (a) The temperature response to a step function forcing scenario in the NorESM model (black curve) and a least squares fit of a power-law expression $\propto t^{\beta/2}$ with $\beta = 0.36$. (b) With $\beta = 0.36$ the response to the deterministic forcing is optimized to fit the global sea surface temperature. The residual signal is analyzed and found consistent with an fGn with exponent $\beta + \beta_f = 0.80$. This gives the estimate $\beta_f = 0.44$. (c) The spatial autocorrelation functions for the sea surface temperatures south of 20°S in a NorESM control run. As in Fig. 10 the solid curves are the theoretical expressions, which in this case are in the form of Eq. (C2). We have estimated $\lambda = 0.41$. (d) The lower black curve is the spectrum of the averaged SO temperature and the red line the power-law spectrum with the estimated exponent β_{cr}. The upper black curve is the average of the local spectra of the SO. Here the red line is the power-law spectrum with exponent $\beta_f + \beta/2 \approx 0.59$.

second harmonic of the annual cycle. We have modeled these trends by the predictor function

$$
\begin{aligned}
y(t) = (a + bt) &+ (c_1 + d_1 t) \sin(2\pi t/100 + \phi_1) \\
&+ (c_2 + d_2 t) \sin(4\pi t/100 + \phi_2),
\end{aligned} \quad (24)
$$

and regressed it to the observation data. The result is the red dotted curve in Fig. 14c. The residual obtained after eliminating the linear and seasonal trends seems to exhibit a power-law spectrum with $\beta \approx 0.5$ on time scales from a month to a decade as shown in Fig. 14d. The PSD has a shape quite similar to the surface temperature over land, and suggests that the radiative CO_2 forcing, and radiative forcing in general exhibits a noisy component that is persistent, and not white. The length of the observation record is too short to claim statistical significance of this persistence on time scales longer than a month, but the noisy CO_2 forcing record illustrates that radiative forcing has a noisy component, and there are good reasons to believe that this noise exhibits persistent scaling properties.

APPENDIX A

Expansion Coefficients for a Random Field

Let $K, N \to \infty$ in Eq. (3) and define

$$
F(\mu, \phi, t) = \lim_{K, N \to \infty} F_{K,N}(\mu, \phi, t).
$$

We form the inner product of each side of this equation with the basis functions $\exp(-i\omega_{j'} t) Y_{n', m'}(\mu, \phi)$ by integrating in time $\int_0^1 dt$ and in space over solid angle $\int_{4\pi} d\Omega = \int_{-1}^{1} d\mu \int_0^{2\pi} d\phi$. By using that these basis functions are orthonormal we find

$$
F(\omega_j, n, m) = \int_0^1 dt \int_{4\pi} d\Omega \, e^{-i\omega t} Y_{n,m}(\mu, \phi) F(\mu, \phi, t). \quad (A1)
$$

Now, let us use Eq. (A1) to compute a covariance of the expansion coefficients:
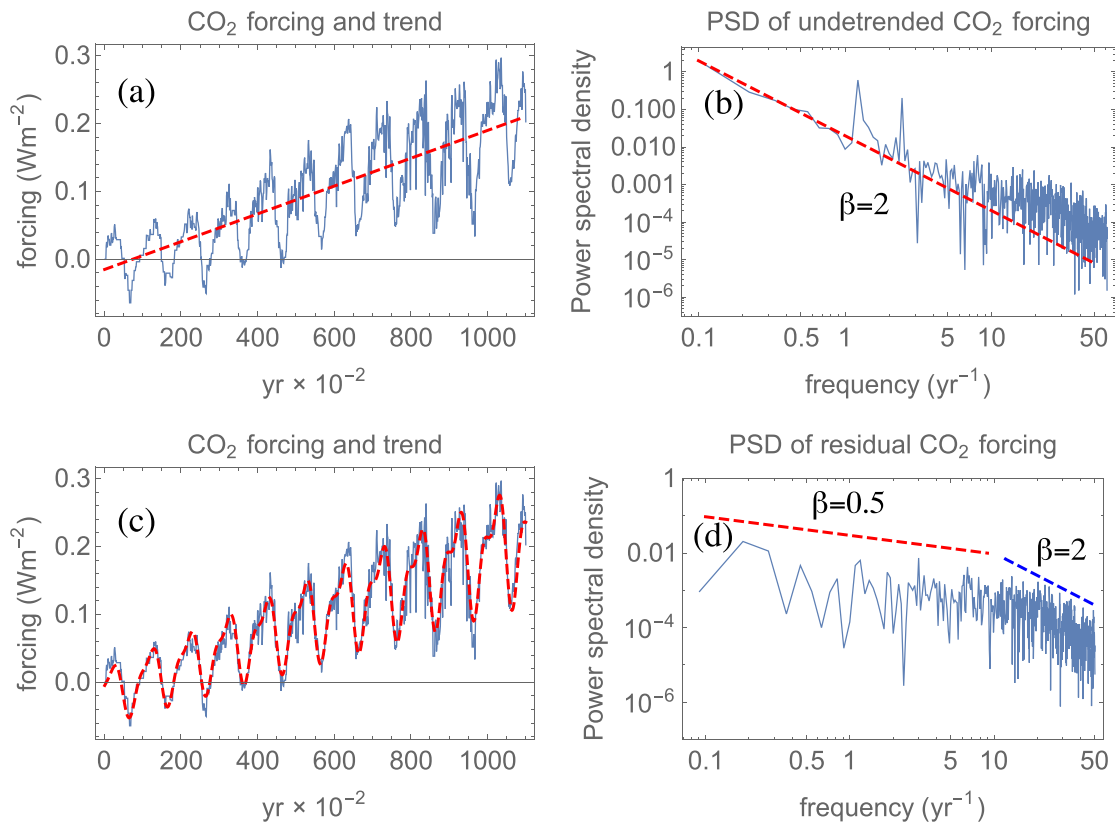
FIG. 14. (a): Measured CO_2 forcing at the surface measured at the North Slope of Alaska from 2000 throughout 2010. Time resolution is 10^{-2} yr. The red dashed line is a linear fit to the data. The slope (trend) is $0.2 \, \mathrm{W\,m}^{-2}$ per decade. (b) The power spectral density (PSD) estimated by the periodogram of the time series in (a). The red dashed line has slope $-\beta = -2$. The slope is strongly influenced by the linear trend. (c) The red dashed curve is a nonlinear regression of the predictor function given by Eq. (24), to the observed time series. (d) The PSD of the residual, defined as the difference between the blue and red curves in (c). The blue dotted line has slope $-\beta = -2$, and the slope of the red dashed line is $-\beta = -0.5$.

$$E[F(\omega_j, n, m)F^*(\omega_{j'}, n', m')] = \int_0^1 dt' \int_0^1 dt' \, e^{-i\omega_j t + i\omega_{j'} t'} \int_{4\pi} d\Omega \int_{4\pi} d\Omega' E[F(\mu, \phi, t)F(\mu', \phi', t')] Y_{n,m}(\mu, \phi, t) Y^*_{n',m'}(\mu', \phi', t').$$

$$(A2)$$

Now we make the assumption of a statistically uniform, random field; that is, we assume that

$$E[F(\mu, \phi, t)F(\mu', \phi', t')] = \sigma^2 \delta(t - t') \delta(\mu - \mu') \delta(\phi - \phi'), \tag{A3}$$

where $\delta(x)$ is the Dirac delta-function and σ is a constant indicating the strength of the field. By substituting Eq. (A3) into Eq. (A2) we find

$$E[F(\omega_j, n, m)F^*(\omega_{j'}, n', m')]$$

$$= \sigma^2 \int_0^1 dt \, e^{-i(\omega_j - \omega_{j'})t} \int_{4\pi} d\Omega \, Y_{n,m}(\mu, \phi, t) Y^*_{n',m'}(\mu, \phi, t)$$

$$= \sigma^2 \delta_{j,j'} \delta_{n,n'} \delta_{m,m'} \tag{A4}$$

and hence

$$E[|F(\omega_j, n, m)|^2] = \sigma^2. \tag{A5}$$

Thus, we have proven the validity of Eq. (4) for a random field.

APPENDIX B

The Spatial Covariance

Here we will prove Eq. (11). By expanding $T(t, \mu, \phi)$ in the same way as in Eq. (3), using Eq. (7) and Eq. (A4), we get

$$C(\mu) = E[T(t,\mu,\phi)T^*(t,1,0)]$$

$$= \sum_{n=0}^{\infty}\sum_{m=-n}^{n}\sum_{n'=0}^{\infty}\sum_{m'=-n'}^{n'} Y_{n,m}(\mu,\phi)Y_{n'm'}(1,0)\sum_{j=-K/2}^{K/2}\sum_{j'=-K/2}^{K/2} e^{i(\omega_{j'}-\omega_j)t}E[F(\omega_j,n,m)F^*(\omega_{j'},n',m')]$$

$$= \sigma^2 \sum_{j=-K/2}^{K/2}\sum_{n=0}^{\infty}\sum_{m=-n}^{n}\frac{Y_{n,m}(\mu,\phi)Y_{n,m}(1,0)}{\omega_j^2\tau_r^2 + [\lambda^2 n(n+1)+1]^2}. \tag{B1}$$

By means of Eqs. (10), (11), and (B1) this reduces to

$$C_{\omega_K}(\mu) = \frac{\sigma^2}{4\pi}\sum_{j=-K/2}^{K/2}\sum_{n=0}^{\infty}\frac{(2n+1)P_n(\mu)}{\omega_j^2\tau_r^2 + [\lambda^2 n(n+1)+1]^2}$$

$$= \sum_{j=-K/2}^{K/2} C_{\omega_j}(\mu)\xrightarrow[K\to\infty]{}\frac{1}{2\pi}\int_{-\infty}^{\infty}C_\omega(\mu)\,d\omega. \tag{B2}$$

The integral on the right-hand side of Eq. (B2) diverges for $\mu = 1$.

The spatial covariance can also be computed directly from Eq. (2). Let us introduce the short-hand notation $\eta = (\mu, \phi)$ and ∇_η^2 the Laplace operator in spherical coordinates given by the second and third terms on the left-hand side of Eq. (2). If we compute each side of Eq. (2) at (η, t) and multiply by $T(\eta', t)$, and then compute each side of Eq. (2) at (η', t), and multiply by $T(\eta, t)$, then addition of the resulting equations yields

$$\frac{\partial}{\partial t}[T(\eta',t)T(\eta,t)] - \lambda^2[T(\eta',t)\nabla_\eta^2 T(\eta,t)$$
$$+ T(\eta,t)\nabla_{\eta'}^2 T(\eta',t)] + 2T(\eta',t)T(\eta,t)$$
$$= T(\eta',t)F(\eta,t) + T(\eta,t)F(\eta',t). \tag{B3}$$

Now, we take the expectation of both sides of Eq. (B3). Stationarity implies that $\partial_t C(\eta', \eta, t) \equiv \partial_t E[T(\eta', t)T(\eta, t)] = 0$, and the white-noise character of the forcing field implies that $E[T(\eta', t)F(\eta, t)] = E[T(\eta, t)F(\eta', t)] = 0$. Thus, the expectation of Eq. (B3) must satisfy the equation

$$\nabla_\eta^2 C(\eta',\eta) + \nabla_{\eta'}^2 C(\eta,\eta') = \frac{2}{\lambda^2}C(\eta',\eta). \tag{B4}$$

The spherical symmetries of the temperature field implies that $\nabla_\eta^2 C(\eta', \eta) = \nabla_{\eta'}^2 C(\eta, \eta')$, and we can without loss of generality set $\eta' \equiv (\mu', \phi') = (1, 0)$. Since covariance only depends on the cosine of the angle between the two vectors η and η', we can then write $C(\eta', \eta) = C(\mu)$, and hence Eq. (B4) reduces to the Legendre equation

$$\nabla^2 C(\mu) \equiv \frac{\partial}{\partial\mu}\left[(1-\mu^2)\frac{\partial C(\mu)}{\partial\mu}\right] = \frac{1}{\lambda^2}C(\mu). \tag{B5}$$

This equation has solutions in the form of the Legendre P_n and Q_n functions, where n is given by $-1/\lambda^2 = n(n+1)$, where n is a nonnegative integer; $P_n(\mu)$ diverges at $\mu = -1$ and $Q_n(\mu)$ at $\mu = 1$. We have already seen that the covariance should diverge at $\mu = 1$, so we should select the solution

$$C(\mu) = A\,\mathrm{Re}\,Q_n(\mu), \tag{B6}$$

with A being a constant and

$$n = \left[\frac{1}{2}\left(-1 + \sqrt{\frac{\lambda^2 - 4}{\lambda^2}}\right)\right].$$

APPENDIX C

Formulation of the Fractional EBM using Fractional Derivatives

The global mean temperature in the fractional EBM is given by convolving the (spatial averaged) forcing $F(t)$ with the power-law kernel given by Eq. (19); that is,

$$T(t) = \xi\int_{-\infty}^{t}\left(\frac{t-s}{\eta}\right)^{\beta/2-1}F(s)\,ds.$$

In practice we have no information about the forcing $F(t)$ in the infinite prehistory, and it is useful to write

$$T(t) = \xi\int_0^t\left(\frac{t-s}{\eta}\right)^{\beta/2-1}[F_0 + F(s)]\,ds, \tag{C1}$$

where F_0 is a parameter describing the deviation from equilibrium at time $t = 0$. We use the following notation for the Riemann–Liouville integral:

$$_aD_t^{-\alpha}f(t) = \frac{1}{\Gamma(\alpha)}\int_a^t(t-s)^{\alpha-1}f(s)\,ds,$$

which allows us to write Eq. (C1) in the form

$$T(t) = \frac{\xi\Gamma(\beta/2)}{\eta^{\beta/2-1}}\,_0D_t^{-\beta/2}[F_0 + F(t)].$$

We have defined

$$c = \frac{2\pi\eta^{\beta/2-1}}{\xi\Gamma(\beta/2)},$$

so the zero-dimensional fractional EBM can be formulated as a fractional differential equation,

$$\frac{c}{2\pi} {}_0D_t^{\beta/2} T(t) = F_0 + F(t).$$

If we consider only purely stochastic forcing the zero can be omitted from the notation on the fractional derivative. Hence, the modification from the zero-dimensional EBM consists of replacing the differential operator $\tau_r \partial_t + 1$ with the fractional operator $D_t^{\beta/2}$. If we apply the same modification to the spatiotemporal model we arrive at

$$\frac{c}{2\pi} D_t^{\beta/2} T - \lambda^2 \nabla^2 T = F.$$

Taking the Fourier transform yields

$$\frac{c}{2\pi} G(\omega)^{-1} T - \lambda^2 \nabla^2 T = F,$$

where $G(t) = \xi(t/\eta)^{\beta/2-1}\Theta(t)$, and thus we arrive at Eq. (22).

ACFs and PSDs in the generalized, fractional EBM

If we replace the white-noise stochastic forcing by a forcing that is fractional in time and white in space, then the relation

$$E[F(\omega,m,n)F^*(\omega,m',n')] = \sigma^2 \delta_{m,m'}\delta_{n,n'}$$

is replaced by the expression

$$E[F(\omega,m,n)F^*(\omega,m',n')] \propto \delta_{m,m'}\delta_{n,n'}\omega^{-\beta_f}.$$

This is actually the expression for the temporal PSD of the forcing noise. From Eq. (16) we then have the following modification of Eq. (17):

$$E[T(\omega,\mu,\phi)T(\omega,\mu',\phi')^*] \propto \omega^{-\beta_f} \sum_{n=0}^{\infty} |g_n(\omega)|^2 (2n+1)P_n(\mu).$$

It follows that

$$S(\omega) = C_\omega(1) \propto \omega^{-\beta_f} \sum_{n=0}^{\infty} |g_n(\omega)|^2 (2n+1). \quad \text{(C2)}$$

When $g_n(\omega)$ is given by Eq. (21) we have

$$\sum_{n=0}^{\infty} |g_n(\omega)|^2 (2n+1) \sim \omega^{-\beta/2}$$

and hence the expression in Eq. (C2) scales as $\sim \omega^{-(\beta/2+\beta_f)}$.

REFERENCES

Bentsen, M., and Coauthors, 2013: The Norwegian Earth System Model, NorESM1-M—Part 1: Description and basic evaluations of the physical climate. *Geosci. Model Dev.*, **6**, 687–720, doi:10.5194/gmd-6-687-2013.

Beran, J., 1994: *Statistics for Long-Memory Processes.* Monographs on Statistics and Applied Probability Series, Vol. 61, Chapman & Hall/CRC, 315 pp.

Brohan, P., J. J. Kennedy, I. Harris, S. F. B. Tett, and P. D. Jones, 2006: Uncertainty estimates in regional and global observed temperature changes: A new data set from 1850. *J. Geophys. Res.*, **111**, D12106, doi:10.1029/2005JD006548.

Budyko, M. I., 1969: The effect of solar radiation variations on the climate of the Earth. *Tellus*, **21**, 611–619, doi:10.1111/j.2153-3490.1969.tb00466.x.

Crowley, T. J., 2000: Causes of climate change over the past 1000 years. *Science*, **289**, 270–277, doi:10.1126/science.289.5477.270.

Feldman, R. D., W. D. Collins, P. J. Gero, M. S. Torn, E. J. Mlawer, and T. R. Shippert, 2015: Observational determination of surface radiative forcing by CO_2 from 2000 to 2010. *Nature*, **519**, 339–343, doi:10.1038/nature14240.

Fraedrich, K., and R. Blender, 2003: Scaling of atmosphere and ocean temperature correlations in observations and climate models. *Phys. Rev. Lett.*, **90**, 108501, doi:10.1103/PhysRevLett.90.108501.

Geoffroy, O., D. Saint-Martin, D. J. L. Olivié, A. Voldoire, G. Bellon, and S. Tytéca, 2013: Transient climate response in a two-layer energy-balance model. Part I: Analytical solution and parameter calibration using CMIP5 AOGCM experiments. *J. Climate*, **26**, 1841–1857, doi:10.1175/JCLI-D-12-00195.1.

Hansen, J., M. Sato, P. Kharecha, and K. von Scuckmann, 2011: Earth's energy imbalance and implications. *Atmos. Chem. Phys.*, **11**, 13 421–13 449, doi:10.5194/acp-11-13421-2011.

Held, I. M., M. Winton, K. Takahashi, T. Delworth, F. Zeng, and G. K. Vallis, 2010: Probing the fast and slow components of global warming by returning abruptly to preindustrial forcing. *J. Climate*, **23**, 2418–2427, doi:10.1175/2009JCLI3466.1.

Iversen, T., and Coauthors, 2013: The Norwegian Earth System Model, NorESM1-M—Part 2: Climate response and scenario projections. *Geosci. Model Dev.*, **6**, 389–415, doi:10.5194/gmd-6-389-2013.

Kantelhardt, J. W., E. Koscielny-Bunde, H. H. A. Rego, S. Havlin, and A. Bunde, 2001: Detecting long-range correlations with detrended fluctuation analysis. *Physica A*, **295**, 441–454, doi:10.1016/S0378-4371(01)00144-3.

Kim, K.-Y., and G. R. North, 1992: Seasonal cycle and second-moment statistics of a simple coupled climate system. *J. Geophys. Res.*, **97**, 20 437–20 448, doi:10.1029/92JD02281.

——, ——, and G. C. Hegerl, 1996: Comparisons of the second-moment statistics of climate models. *J. Climate*, **9**, 2204–2221, doi:10.1175/1520-0442(1996)009<2204:COTSMS>2.0.CO;2.

Mann, M. E., 2011: On long-range dependence in global temperature series. *Climatic Change*, **107**, 267–276, doi:10.1007/s10584-010-9998-z.

Moberg, A., D. M. Sonechkin, K. Holmgren, N. M. Datsenko, and W. Karlen, 2005: Highly variable Northern Hemisphere temperatures reconstructed from low- and high-resolution proxy data. *Nature*, **433**, 613–617, doi:10.1038/nature03265.

North, G. R., and R. F. Cahalan, 1981: Predictability in a solvable stochastic climate model. *J. Atmos. Sci.*, **38**, 504–513, doi:10.1175/1520-0469(1981)038<0504:PIASSC>2.0.CO;2.

——, J. Wang, and M. G. Genton, 2011: Correlation models for temperature fields. *J. Climate*, **24**, 5850–5862, doi:10.1175/2011JCLI4199.1.

Østvand, L., T. Nilsen, K. Rypdal, D. Divine, and M. Rypdal, 2014: Long-range memory in internal and forced dynamics of millennium-long climate model simulations. *Earth Syst. Dyn.*, **5**, 295–308, doi:10.5194/esd-5-295-2014.

Rypdal, K., 2012: Global temperature response to radiative forcing: Solar cycle versus volcanic eruptions. *J. Geophys. Res.*, **117**, D06115, doi:10.1029/2011JD017283.

——, and M. Rypdal, 2014: Long-memory effects in linear-response models of Earth's temperature and implications for future global warming. *J. Climate*, **27**, 5240–5258, doi:10.1175/JCLI-D-13-00296.1.

——, L. Østvand, and M. Rypdal, 2013: Long-range memory in Earth's surface temperature on time scales from months to centuries. *J. Geophys. Res. Atmos.*, **118**, 7046–7062, doi:10.1002/jgrd.50399.

Sellers, W. D., 1969: A global climatic model based on the energy balance of the Earth–atmosphere system. *J. Appl. Meteor.*, **8**, 392–400, doi:10.1175/1520-0450(1969)008<0392:AGCMBO>2.0.CO;2.